IEEE Open Journal of
Antennas and Propagation

Received 23 December 2021; revised 4 February 2022; accepted 6 February 2022. Date of publication 9 February 2022; date of current version 17 February 2022.

Digital Object Identifier 10.1109/OJAP.2022.3150100

Experimental Validation of the DBIM-TwIST Algorithm for Brain Stroke Detection and Differentiation Using a Multi-Layered Anatomically Complex Head Phantom

OLYMPIA KARADIMA[1], PAN LU[1], IOANNIS SOTIRIOU[1,2], AND PANAGIOTIS KOSMAS[1,2], (Senior Member, IEEE)

[1]Department of Engineering, Faculty of Natural and Mathematical Sciences, King's College London, London WC2R 2LS, U.K.

[2]Meta Materials Inc., Dartmouth, NS B2Y 4M9, Canada

CORRESPONDING AUTHOR: O. KARADIMA (e-mail: olympia.karadima@kcl.ac.uk)

This work was supported by the EMERALD Project funded from the European Union's Horizon 2020 Research and Innovation Programme through the Marie Skłodowska-Curie under Grant 764479.

ABSTRACT We present an experimental validation of the distorted Born iterative method with the two-step iterative shrinkage thresholding (DBIM-TwIST) algorithm for the problem of brain stroke detection and differentiation, using an anatomically accurate, multi-layer head phantom. To this end, we have developed a gelatine-based, anatomically complex head phantom which mimics various brain tissues and also includes a target mimicking hemorrhagic or ischemic stroke. We simulated the model and setup using CST Microwave Studio and then used our experimental imaging setup to collect numerical and measured data, respectively. We then used our DBIM-TwIST algorithm to reconstruct the dielectric properties of the imaging domain for both simulated and measured data. Results from our CST simulations showed that we are able to locate and reconstruct the permittivity of different stroke targets using an approximate initial guess. Our experimental results demonstrated the potential and challenges for successful detection and differentiation of the stroke targets.

INDEX TERMS Distorted born iterative method, inverse scattering, microwave tomography, stroke detection.

I. INTRODUCTION

CEREBROVASCULAR accidents (brain strokes) are among the leading causes of death and disability worldwide [1]. Brain strokes are caused by a ruptured (hemorrhagic) or a blocked (ischemic) vessel. Determining the stroke type as early as possible is crucial, as the wrong or delayed treatment could be lethal [2]. Currently, magnetic resonance imaging (MRI) and computed tomography (CT) scans are widely used as acute-care imaging methods for stroke detection [3]. However, their use for pre-clinical diagnosis or continuous monitoring is limited by cost, size and mobility [4]. Furthermore, safety concerns have been raised regarding the ionized radiation emitted by CT scans [5]. The above challenges motivated the development of novel imaging methods that aspire to be fast, safe, portable and cost-effective. Microwave imaging (MWI) [6] is among the candidates to satisfy these requirements towards detecting and monitoring brain stroke in the pre-hospital or post-acute stage.

MWI exploits the dielectric contrast between different human tissues [7], [8]. In the last 40 years, extended research has been conducted towards the development of MWI systems for various medical conditions like breast cancer and brain stroke detection [9]–[24]. For brain stroke detection and classification, human trials have been reported in [14], [22] and [24]. An auspicious case report by [25]

presented images from a novel, portable electromagnetic scanner used in patients with either hemorrhagic or ischemic stroke. The presented images are encouraging. However, while such clinical studies are the main target for MWI stroke detection, they cannot be used to fully evaluate the accuracy in estimating the dielectric properties of the stroke and hence the system's ability to differentiate hemorrhagic from ischemic stroke. The problem has also been studied using inverse problems theory such as in [26] and [27], which showed that the optimal frequency range and number of antennas for a MWI head scanner should be 0.5–2.0 GHz and 24, respectively.

MWI techniques for the brain include microwave tomographic (MWT) and radar approaches [28]. Radar methods produce maps of backscattered energy [28]–[30], while MWT reconstructs the dielectric properties of the unknown region by solving an inverse scattering electromagnetic (EM) problem [11], [31]. Hybrid methods have also been proposed as in [32], which uses information from a radar-based algorithm to locate the target and then applies MWT to estimate the brain's and target's dielectric properties. Machine learning approaches have also been proposed for brain stroke classification and they have shown to be potentially fast, robust, and accurate [22], [33]–[36]. More specifically, [37] conducted animal experiments using a non-contact microwave-based stroke detection system for classifying the type of the stroke, as well as monitoring the severity and the progress of the stroke by using different metrics. The main disadvantage of the above-mentioned approaches is the lack of images which could limit their clinical adoption. Moreover, machine learning methods require large data-sets, which are difficult to obtain for a technology that is yet to be clinically adopted.

MWT algorithms for brain imaging face two main challenges: the increased anatomic complexity of the head combined with high dielectric contrast between individual tissues, and the need for a robust algorithm that can overcome the non-linearity and ill-posedness of the resulting inverse problem [38]. To assess MWT performance against these challenges, numerical and experimental phantoms that mimic the structure and dielectric properties of the brain have been developed, e.g., [39]. While the dielectric properties of normal brain tissues have been widely reported [7], [8], there is little information on the dielectric properties of ischemic tissues. To the best of our knowledge, [40] is the only study that measured the dielectric properties of ischemia-infected areas ex-vivo. In this paper, it was reported that the properties of ischemic tissues vary from -10 to -25% in comparison with the dielectric properties of healthy brain tissue.

Several solutions have been proposed and compared (e.g., [9], [41]) to deal with the EM inverse scattering problem. In [33], a multi-step learning-by-examples strategy has been presented and validated for brain stroke detection, identification, and localization, using a simplified head phantom made by and octagonal prism filled with the dielectric properties of average brain and with circular cylinders which mimic the two types of the stroke. The study in [42] presented a novel non-linear S-Parameters inversion method for stroke imaging based on Lebesgue spaces with non-constant exponents. The experimental prototype included a liquid-filled 3-D SAM phantom which mimics the dielectric properties of average brain in the presence of a stroke-like target. The presented simulation and experimental results at 1 GHz were very promising, but a further assessment of the method using a multi-layered phantom in a wider frequency range is needed. The distorted Born iterative method with the two-step iterative shrinkage/thresholding (DBIM-TwIST) linear inverse solver has been proposed in [43]. Recently, the algorithm has been used to reconstruct images from experimental or numerical three-dimensional (3-D) data [44], and it has been tested with both finite-difference time-domain (FDTD) as well as finite element method (FEM)-based forward solvers [45].

Three-dimensional (3-D) MWT algorithms in medical imaging have been presented in [31], [46]–[48] but mainly for breast imaging. For the problem of head imaging, [49], [50] used scattered signals from 3-D head phantoms applying FDTD and FEM, respectively, while [9] suggested incorporating FEM with TSVD. Moreover, recent work [44] presented a 3-D DBIM implementation combined with the fast iterative shrinkage/thresholding algorithm (FISTA), which showed promise in imaging complex numerical head models. We have also validated experimentally our two-dimensional (2-D) DBIM-TwIST algorithm and imaging system with simplified head phantoms, for which we showed our method's potential to differentiate stoke types [18].

The aim of this paper is to experimentally validate further our 2-D and 3-D DBIM-TwIST algorithms for stroke detection and differentiation using a novel multi-layer head phantom. To this end, we have developed a new realistic phantom that mimics the head anatomy, which is derived from to the MRI-based, numerical phantom [51]. We then surrounded this "Zubal" phantom with a 3-D array of antennas immersed in our imaging prototype presented in [18], [19], and we obtained numerical (via CST Microwave Studio) and experimental data. Our results demonstrate the potential of reconstructing successfully the dielectric properties of different targets when only an approximation of the head phantom is known *a priori*.

The remainder of the paper is organized as follows: Section II details the methodology of constructing the "Zubal" head phantom and its properties, and presents the DBIM-TwIST algorithm and 3-D data acquisition process. Section III presents our numerical and experimental results for hemorrhagic and ischemic stroke-like targets, followed by Section IV which discuses our findings and explores our future work.

II. METHODOLOGY

A. HEAD PHANTOM CONSTRUCTION

We derived our Zubal phantom from a 2-D axial $x-y$ slice taken from the original MRI-derived Zubal head phantom [51], which was then extended by a few cm along

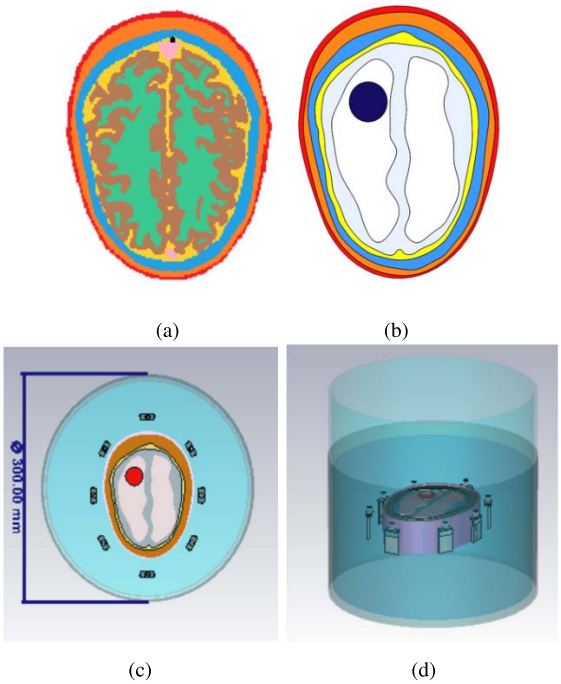

FIGURE 1. (a) The Zubal head model section; (b) Simplified CAD model for fabrication; (c) Top view of the Zubal model on CST; (d) Side view of the Zubal model on CST. The phantom includes the following head layers: Skin, bone, CSF, grey matter, white matter and the target.

the z axis. We imported this 3-D model in CAD software to simplify its structure so that it is easy to fabricate and work with, without sacrificing much of its complexity (Fig. 1(a) and Fig. 1(b)). For our simulation, we imported the CAD model on CST which from now on we will refer to as the "Zubal model". The simulated phantom and setup are shown in Fig. 1(c) and Fig. 1(d). We filled each layer of the phantom with the dielectric properties of different head tissues having created a anatomically accurate 5-material head model. We placed a cylindrical target at the top right, inside the white matter area, with radius $\rho = 12.5$ mm and height h $= 100$ mm. The phantom was immersed in our imaging setup presented in [18], which includes eight antennas placed in an elliptical array configuration with major and minor axes equal to 205 mm and 148 mm, respectively.

To validate our algorithm experimentally, we prepared a novel gelatine-based head phantom in accordance with the anatomy and the dimensions of the Zubal model. The mould form consists of six compartments which create the sequence of the tissue mimicking materials needed for our assembly. The moulds were fabricated using a Zortrax M200 FDM 3-D printer in a complementary manner using two moulds showed in Fig. 2(a) and Fig. 2(b). This methodology for the creation of the phantom allows a more accurate validation as it avoids the presence of 3-D printed infill patterns that irregularly encapsulate fluids. The adverse effect of the presence of plastic in phantoms which use it as support was demonstrated in [52].

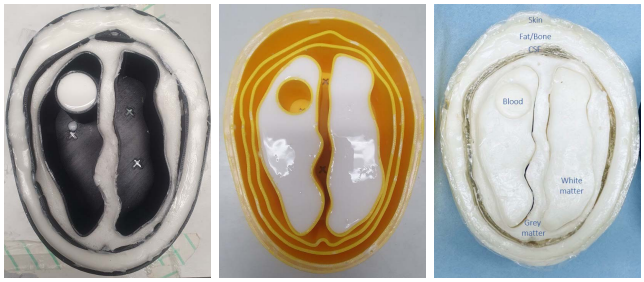

FIGURE 2. Top view of the moulds constructing the Zubal head phantom from gelatine-based tissue mimicking materials: (a) First mould (bone, grey matter, and target); (b) Second mould (skin, CSF and white matter); (c) Final phantom with five tissues and target.

FIGURE 3. Demoulding process.

Having prepared the tissue-mimicking gels, we poured them in the desired compartments in Fig. 2(a) and Fig. 2(b), and we allowed them to dry for at least 8 hours depending on their concentration. To extract the gels from the moulds we initially submerged the moulds in warm water so the outer layers could slide out easier, whilst we were applying small amount of air pressure at the lower part of the mould (Fig. 3). Once the gels were extracted, we stacked the materials within each other and wrapped the assembly using a thin plastic film to prevent it from drying. The final Zubal model is presented in Fig. 2(c).

We prepared the tissue-mimicking materials for skin, bone, cerebrospinal fluid (CSF), grey matter, white matter, blood and ischemia by following the process presented in [18]. Table 1 shows the concentrations of the materials used for preparing each layer of the phantom.

Fig. 4 displays the measured dielectric properties of the prepared phantoms for skin, bone, grey matter, white matter and ischemia, respectively. We note that the figure does not report the measured properties of CSF/h-stroke, as the material was not set at the time of the dielectric measurements. The preparation of CSF/h-stroke does not require the addition of oil, which is the most challenging step in the preparation process and can lead to variations in the final dielectric

TABLE 1. Concentrations of materials used for 100 ml of tissue mimicking phantoms. For each tissue mimicking phantom we also use 1 ml of propanol and 1 ml of surfactant.

	Water	Gelatine powder	Kerosene + Safflower oil
Skin	73 ml	13 gr	15 ml
Bone	45 ml	5 gr	50 ml
CSF/h-stroke	80 ml	17 gr	- ml
Grey matter	75 ml	12 gr	13 ml
White matter	70 ml	10 gr	20 ml
i-stroke	55 ml	10 gr	35 ml

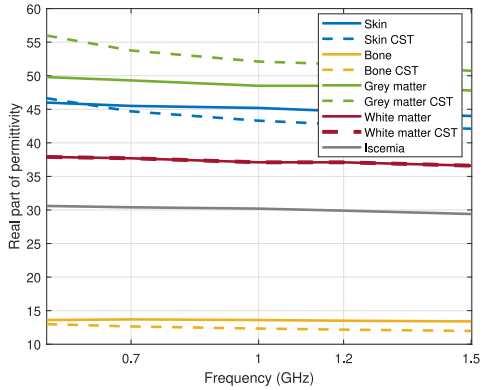

(a)

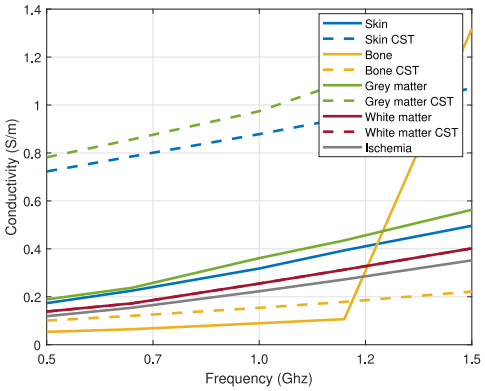

(b)

FIGURE 4. Measured dielectric properties of the produced tissue mimicking materials against reference values taken from CST: (a) permittivity, and (b) conductivity. Note that there appears to be a measurement error for the bone phantom above 1.2 GHz.

properties of the phantoms. Preparing phantoms that mimic the dielectric properties of CSF or h-stroke requires only dissolving the gelatine within the water. Therefore, we can safely assume that we can achieve the properties reported at [18]. For the CSF/h-stroke fabricated phantom of [18] the permittivity at 1 GHz is 68, while the conductivity is 0.3 S/m and 1.2 S/m for h-stroke and CSF respectively. The measurements were performed using Keysight's dielectric spectroscopy kit, over a 0.5-1.5 GHz frequency range at different points. The plots reveal a very good agreement with the reference permittivity taken from CST (Fig. 4(a)), but lower conductivity values for skin and grey matter phantoms (Fig. 4(b)). As there is no literature regarding the dielectric properties of ischemia in a wide frequency range, we made

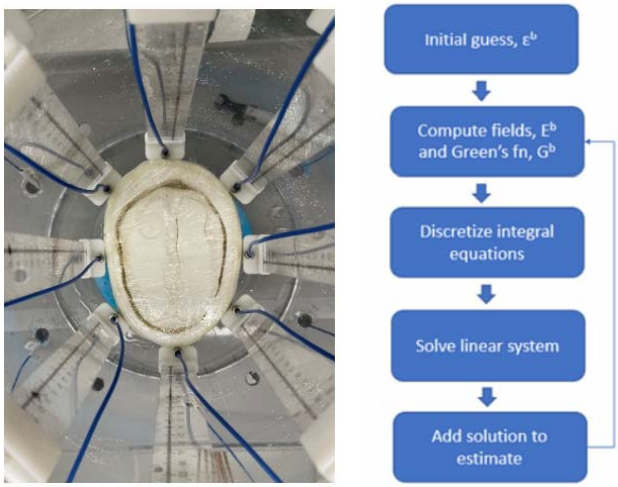

(a) (b)

FIGURE 5. (a): The imaging tank with the immersed Zubal model. (b): Flowchart of the DBIM method.

the assumption that the ischemic properties are 25% less than the dielectric properties of healthy brain tissue [40].

B. IMAGING METHODOLOGY

The Zubal model was positioned in the middle of the 300 mm diameter cylinder tank, as shown in Fig. 5(a). It was surrounded by eight spear-shaped antennas [19] in an elliptical array, and the imaging tank was filled with 90% glycerol-water. The choice of the antenna number, as well as the choice of the matching medium have been extensively reported in [18]. The tank was made of acrylic and was surrounded by an absorber (ECCOSORB MCS) which was confined by a metallic shield. The setup was surrounded by vacuum and the measurements were performed in the frequency range of 0.5 to 1.5 GHz. For every studied case, two scenarios were examined. First, we considered a scenario without a target ("NT"), where the target area was filled with the dielectric properties of the white matter. For the "WT" scenario we filled the equivalent target territory (radius $\rho = 12.5$ mm and height h $= 100$ mm) with the dielectric properties either of blood or of ischemia. For each scenario and for M frequency points, the eight antenna-array captured the MWT data, resulting into a 8x8xM scattering matrix, which was then fed and processed by our algorithm.

The 2-D version of DBIM has been described extensively in our previous work, such as [18]. More specifically, DBIM solves the EM integral equation under the distorted Born approximation at each iteration as follows:

$$\begin{aligned} E_s(r_n, r_m) &= E_t(r_n, r_m) - E_b(r_n, r_m) \\ &= \omega^2 \mu \int_V G_b(r_n, r) E_b(r, r_m)(\epsilon(r) - \epsilon_b(r) dr) \end{aligned} \tag{1}$$

where E_t, E_s and E_b are the total, scattered and background fields respectively, while r_n and r_m indicate the

TABLE 2. Debye parameters of the forward model.

Material type	$\Delta\epsilon$	ϵ_∞	σ_s
90% glycerol-water	6.56	16.86	0.3232
Average brain	45.8	0.1244	0.7595

transmitter and receiver positions and G_b denotes the Green's function for the background medium. The contrast function $(\epsilon(r)-\epsilon_b(r))$ indicates the dielectric difference between the reconstructed and the background complex permittivity. Both E_b and G_b, are calculated with a forward solver based on the finite-difference time-domain (FDTD) method [43]. While (1) is a two-dimensional TM integral equation, it can be used to implement the 3-D DBIM if we consider that only electric fields along the polarization direction of the antennas are significant [31], [44]. To overcome the ill-posedennes of the linear system resulting from discretizing (1) at each DBIM iteration, we use the two-step iterative shrinkage thresholding (TwIST) method which splits the matrix into a two-step iterative equation. The contrast function is calculated iteratively and is added to the background profile until a convergence is reached [18]. A flowchart of the method is presented at Fig. 5(b).

Our forward model consists of both a 2-D and 3-D depiction of the set-up for the two versions of the DBIM-TwIST respectively. It includes the tank filled with the dielectric properties of 90% glycerol-water and an ellipsoid that represents the Zubal model filled with the dielectric properties of the average brain. The axes of the 2-D ellipsoid are 153 mm and 112 mm long and they represent the actual size of the phantom's axial slice at the height where the antennas are located. The dimensions of the 3-D ellipsoid are 170x130x100 mm long.

As the forward models are simplified versions of our experiment, they are not identical and hence there are differences between the real and the FDTD simulated models. The algorithm simulates the setup's antennas with line sources placed at the same location as their feeding point. To minimize the mismatch between the simulation or the experiment and the forward model, we calibrated our forward model by employing a "no target" scenario, as in our previous work (e.g., [18]). We calculated the signal difference between the inverse and the forward "no target" cases and we used this difference to calibrate the scattered data taken from the "with target" scenario.

To model the frequency-depended behavior of the human tissues, we applied the single-pole Debye model for the complex permittivity ϵ_b [18]. Table 2 presents the Debye parameters of the "initial guess" model that were used with the FDTD forward solver to calculate the 2-D (transverse magnetic wave) and 3-D (full wave) fields. The calculation of full wave fields is the main difference between the 2-D and the 3-D version of the algorithm. The Debye parameters are calculated and updated at each iteration until we reach a fixed number of iterations or the difference between the "measured" and calculated electric fields is minimized. We employ DBIM-TwIST to reconstruct the Debye parameters with a 2 mm resolution grid. We have observed that the reconstructed results do not improve significantly when we apply more than 20 iterations, and hence we chose to perform 20 DBIM iteration for both 2-D and 3-D versions of DBIM-TwIST. This number is a trade-off between the accuracy and the total execution time.

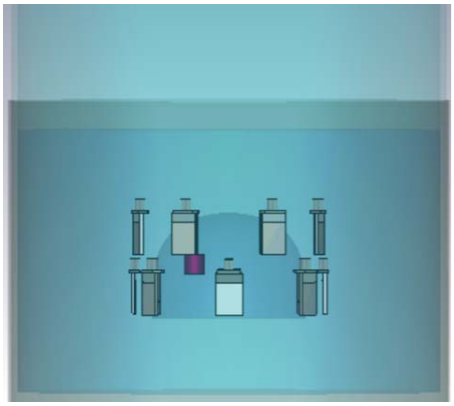

FIGURE 6. CST model of a simplified brain phantom surrounded by 16 antennas in 2 elliptical arrays.

For the 3-D code, we employed the Nvidia GPU Tesla K20c to accelerate the 3-D FDTD execution with CUDA, and MATLAB MEX functions to incorporate the GPU code with the DBIM code in MATLAB. The environment was based on MATLAB R2020b, CUDA 8.0 and VS 2015. The implementation of DBIM-TwIST with a GPU-based FDTD forward solver was extensively described in [44]. By the means of an example, using the 3-D DBIM-TwIST, for the case of the Zubal model with h-stroke, the elapsed time for each antenna is 81 seconds, meaning that the running time for each iteration is roughly 11 minutes when using 8 monopole antennas. For the 2-D code we do not need GPU acceleration for the forward solver. The running time for each iteration, when using 8 antennas, is 12 seconds using MATLAB R2020b on an Intel i7 processor with 16 GB RAM memory.

III. COMPARISON OF 2-D AND 3-D DBIM-TWIST FOR A 3-D IMAGING PROBLEM

In this section we present an initial validation and assessment of the 3-D algorithm for the case of a simplified homogeneous elliptical brain phantom in the presence of a small stroke-like target, surrounded by a 3-D antenna array arranged in two cylindrical rings. We also compare the capabilities of the 2-D and 3-D versions of the algorithm to confirm the hypothesis that 3-D DBIM-TwIST can result in more accurate reconstructions for 3-D inverse problems.

Fig. 6 illustrates the brain phantom immersed in our imaging setup presented at [18]. The phantom is surrounded by 16 monopole antennas in two different arrays, which form two offset rings of 8 elements each. To mimic the h-stroke or the i-stroke, we have examined the same configuration in

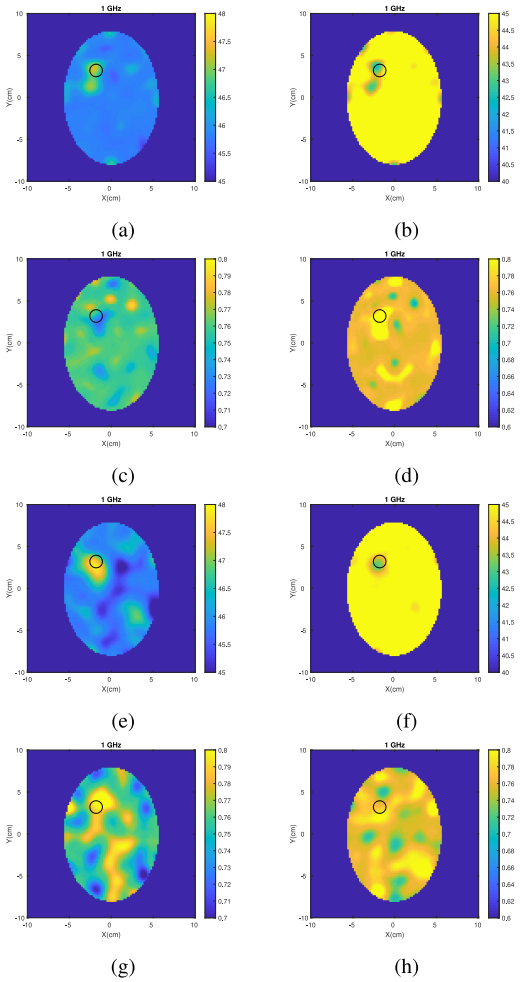

FIGURE 7. First row: Reconstructed permittivity for the phantom of Fig. 6, for h- and i-stroke using 2-D DBIM-TwIST and the bottom array of antennas; Second row: Reconstructed conductivity for the phantom of Fig. 6, for h- and i-stroke using 2-D DBIM-TwIST and the bottom array of antennas; Third row: Reconstructed permittivity for the phantom of Fig. 6, for h- and i-stroke using 2-D DBIM-TwIST and the top array of antennas; Fourth row: Reconstructed conductivity for the phantom of Fig. 6 for h- and i-stroke using 2-D DBIM-TwIS and the top array of antennas.

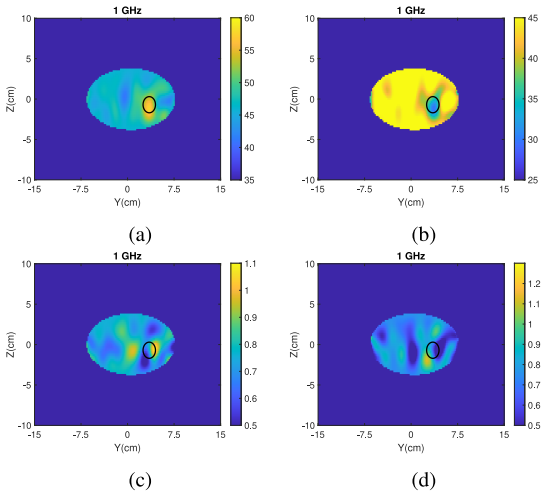

FIGURE 8. First row: Y-Z slice of 3-D reconstructed permittivity for the phantom of Fig. 6 for h- and i-stroke; Second row: Y-Z slice of 3-D reconstructed conductivity for the phantom of Fig. 6 for h- and i-stroke.

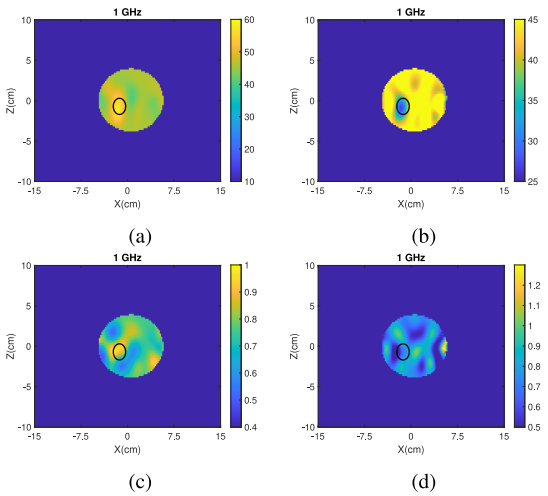

FIGURE 9. First row: X-Z slice of 3-D reconstructed permittivity for the phantom of Fig. 6 for h- and i-stroke; Second row: X-Z slice of 3-D reconstructed conductivity for the phantom of Fig. 6 for h- and i-stroke.

the presence of a 20 mm diameter and 20 mm height target, located between the two heights of the antennas. The Debye parameters of the target and of the average brain have been assigned by curve fitting from CST data [53]. As explained in our Methodology section, the inverse model used in our imaging algorithm considers a 2-D (112 × 153 mm), or a 3-D (112 × 153 × 100 mm) ellipsoid, for the two versions of the algorithm respectively. The algorithm considers point sources which form an elliptical array and are located at the same height in 3-D case as the antennas in the CST simulation.

Figs. 7–10 present the reconstructed permittivity and conductivity at 1.0 Ghz for the phantom of Fig. 6 for h- and i-stroke respectively, using both 2-D and 3-D versions of the DBIM-TwIST. More specifically, Fig. 7 shows the 2-D reconstructed permittivity and conductivity using either the top or the bottom array of antennas in our forward model. Figs. 8–10 demonstrate the sagittal, axial and coronal planes at y-z, x-z and x-y slices from the 3-D reconstructions, respectively.

We observe that both versions of the algorithm can successfully locate and detect the dielectric permittivity of the target. However, the 3-D algorithm achieves more accurate results for both cases of stroke, as it combines information from both rings in an efficient way. Importantly, the 3-D DBIM-TwIST leads to a clear improvement in estimating the target's conductivity relative to 2-D reconstruction based on either ring. Having established the benefits of 3-D imaging, our subsequent results focus on validating the 3-D DBIM-TwIST experimentally, as well as compare its performance with the 2-D version of the algorithm. The experimental setup and respective CST model, however, does not include two antenna rings due to the smaller size of the experimental phantom. In this respect, the setup in these results resembles

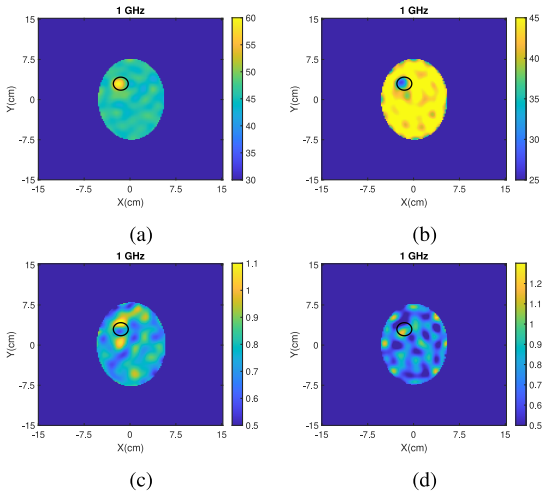

FIGURE 10. First row: X-Y slice of 3-D reconstructed permittivity for the phantom of Fig. 6 for h- and i-stroke; Second row: X-Y slice of 3-D reconstructed conductivity for the phantom of Fig. 6 for h- and i-stroke.

a 2-D configuration, but the 3-D results are still relevant as they are derived from the 3-D algorithm which reconstructs a fully 3-D region.

IV. RESULTS WITH THE ZUBAL PHANTOM

This section presents reconstruction results from our Zubal model in the presence of a hemorrhagic and an ischemic stroke. Our aim was to assess our imaging system's ability to determine the type of stroke from estimating its dielectric properties using the 2-D and 3-D DBIM-TwIST algorithm. We have examined both CST-calculated and experimental data, and we have compared our 2-D and 3-D results. As previous work in MWT has shown that thermal noise does not affect reconstruction quality as much as the mismatch between the true experiment and the inverse model, we did not include noise in the CST data, to focus on the effect of the model mismatch errors [11], [43]. To compare the quality of the reconstructed images we calculated the relative errors of the permittivity and conductivity in the target area at each iteration, as follows:

$$error_{permittivity} = \frac{\left\|\epsilon_{original} - \epsilon_{reconstructed}\right\|^2}{\left\|\epsilon_{original}\right\|^2} \quad (2)$$

$$error_{conductivity} = \frac{\left\|\sigma_{original} - \sigma_{reconstructed}\right\|^2}{\left\|\sigma_{original}\right\|^2}. \quad (3)$$

A. RECONSTRUCTIONS WITH CST DATA

Two CST simulations were conducted to acquire the scattered field data, with and without the target. The dielectric properties of each tissue were imported from the CST library. Specifically for the ischemic target, as there are not frequency-dependence reported values in the literature, we used our measured dielectric properties reported at [18].

Fig. 11 and Fig. 12 present the reconstructed permittivity and conductivity at four frequencies for the Zubal model of Fig. 1 inside our prototype, in the presence of h-stroke and i-stroke targets. More specifically, Fig. 11 shows the reconstructed permittivity and conductivity for the 2-D version of DBIM-TwIST, while Fig. 12 shows the equivalent reconstructed dielectric properties for the 3-D version. Overall, more accurate results are produced for the lower frequencies of 0.9 and 1.0 GHz, and artifacts increase significantly for frequencies above 1.0 GHz. This can be attributed to the increased non-linearity of the EM inverse scattering problem in higher frequencies, where multiple scattering effects become stronger. To include higher frequencies for enhanced resolution, a multiple-frequency inversion approach can be adopted [43].

We also observe that there is a clear distinction in the estimation of the permittivity for the two targets for both versions of the code. For 2-D DBIM-TwIST, the results of Fig. 11 estimate the value of permittivity ϵ' at 1.0 GHz as $\epsilon' = 50.31$ and $\epsilon' = 43.15$ for hemorrhagic and ischemic stroke, respectively. For the 3-D DBIM-TwIST, Fig. 12 shows that the equivalent values of permittivity are $\epsilon' = 61.58$ and $\epsilon' = 28.52$, respectively. We also observe that 3-D DBIM-TwIST estimates more accurately the reconstructed values for the target area. The equivalent reconstructions of Fig. 11 reveal that we are not able to successfully detect the target from the conductivity reconstructions. The quality of conductivity reconstructions improves using the 3-D DBIM-TwIST algorithm, for which the reconstructed conductivity values are significantly different for the two stroke-type targets.

B. RECONSTRUCTIONS WITH EXPERIMENTAL DATA

Fig. 13 and Fig. 14 present complex permittivity reconstructions in the presence of the hemorrhagic or ischemic stroke target, using measured data and the 2-D and 3-D DBIM-TwIST, respectively. These images suggest that we are able to detect and estimate the dielectric properties of h-stroke for both versions of the algorithm. The 3-D DBIM-TwIST reconstructions of the permittivity have more artifacts that could be misleading regarding the target location in the absence of a-priori information. Interestingly, the 3-D version of the algorithm leads to conductivity reconstructions with less artifacts than the equivalent permittivity results for the h-stroke case at lower frequencies. Permittivity values at 1.0 GHz are $\epsilon' = 51.6$ and $\epsilon' = 61.57$, for the 2-D and 3-D DBIM-TwIST respectively. However, we observe artifacts in the reconstruction images for reconstructions with the ischemic stroke. More specifically and as shown in Figs. 13(i)–13(l) and Figs. 14(i)–14(l), we are able to detect an area with values lower than the average brain, which is close to the target area. There is an offset, however, between the location of the real and the detected target. The results in Figs. 13(m)–13(p) and Figs. 14(m)–14(p) for the conductivity reconstructions reveal similar tendencies.

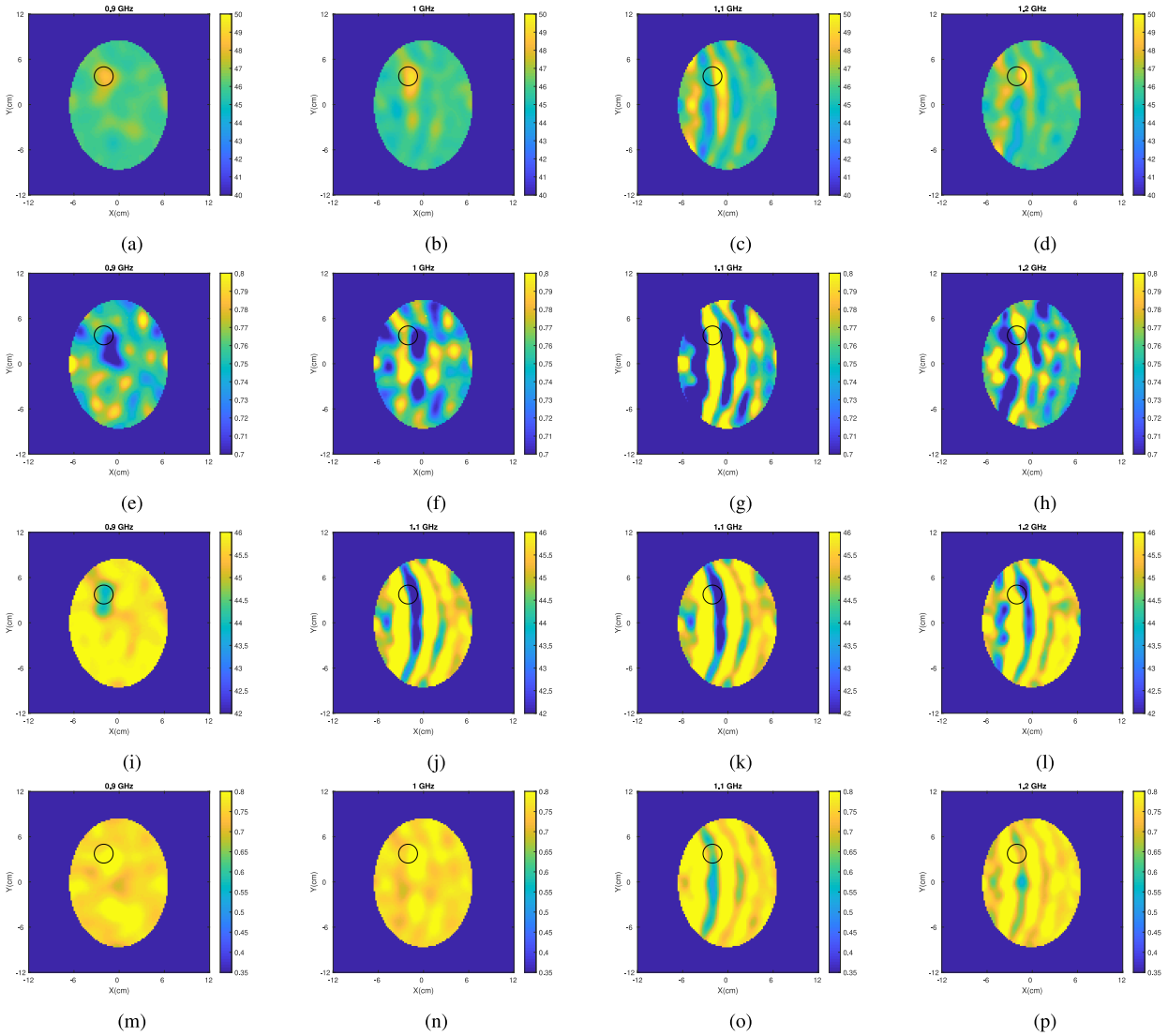

FIGURE 11. First row: CST reconstructed results of the permittivity for h-stroke using 2-D DBIM-TwIST; Second row: CST reconstructed results of the conductivity for h-stroke using 2-D DBIM-TwIST; Third row: CST reconstructed results of the permittivity for i-stroke using 2-D DBIM-TwIST; Fourth row: CST reconstructed results of the conductivity for i-stroke using 2-D DBIM-TwIST.

The dielectric difference observed between the i-stroke and the white matter is less than the dielectric difference between the h-stroke and the white matter, resulting in a more complex brain structure. In addition, differences between our experimental model and the FDTD forward model, in combination with different software environments, result in significant model mismatch. Overall, both 2-D and 3-D algorithms have detected accurately the h-stroke, although we observe more artifacts for the 3-D version. Overall, experimental measurement errors lead to less accurate reconstructions than their CST equivalent.

The error metrics calculated by (2) and (3) can be used to evluate the accuracy of the reconstruction. These errors are summarized in Tables 3–6. We observe that relative errors fall below 1 for all cases except from the conductivity errors of the 2-D i-stroke cases, as well as the 3-D i-stroke scenarios, where image artifacts are dominant. The high conductivity errors for the 2-D experimental i-stroke suggest that the estimation of the target is not accurate. This is due to an offset between the real and the reconstructed target area for the experimental i-stroke reconstructions. The lowest values are observed for the cases of 2-D and 3-D h-stroke with CST data, at 1 and 0.9 GHz, respectively. Comparing all the images, these are the scenarios with the best estimated reconstructed target and the weakest artifacts.

TABLE 3. Relative errors of the permittivity in the target area for the 2-D examined scenarios.

	0.9 GHz	1.0 GHz	1.1 GHz	1.2 GHz
CST h-stroke	0.2051	0.1877	0.2259	0.2121
CST i-stroke	0.7853	0.7595	0.7843	0.8303
Exp h-stroke	0.1951	0.1929	0.1944	0.1460
Exp i-stroke	0.8613	0.8524	0.8465	0.8414

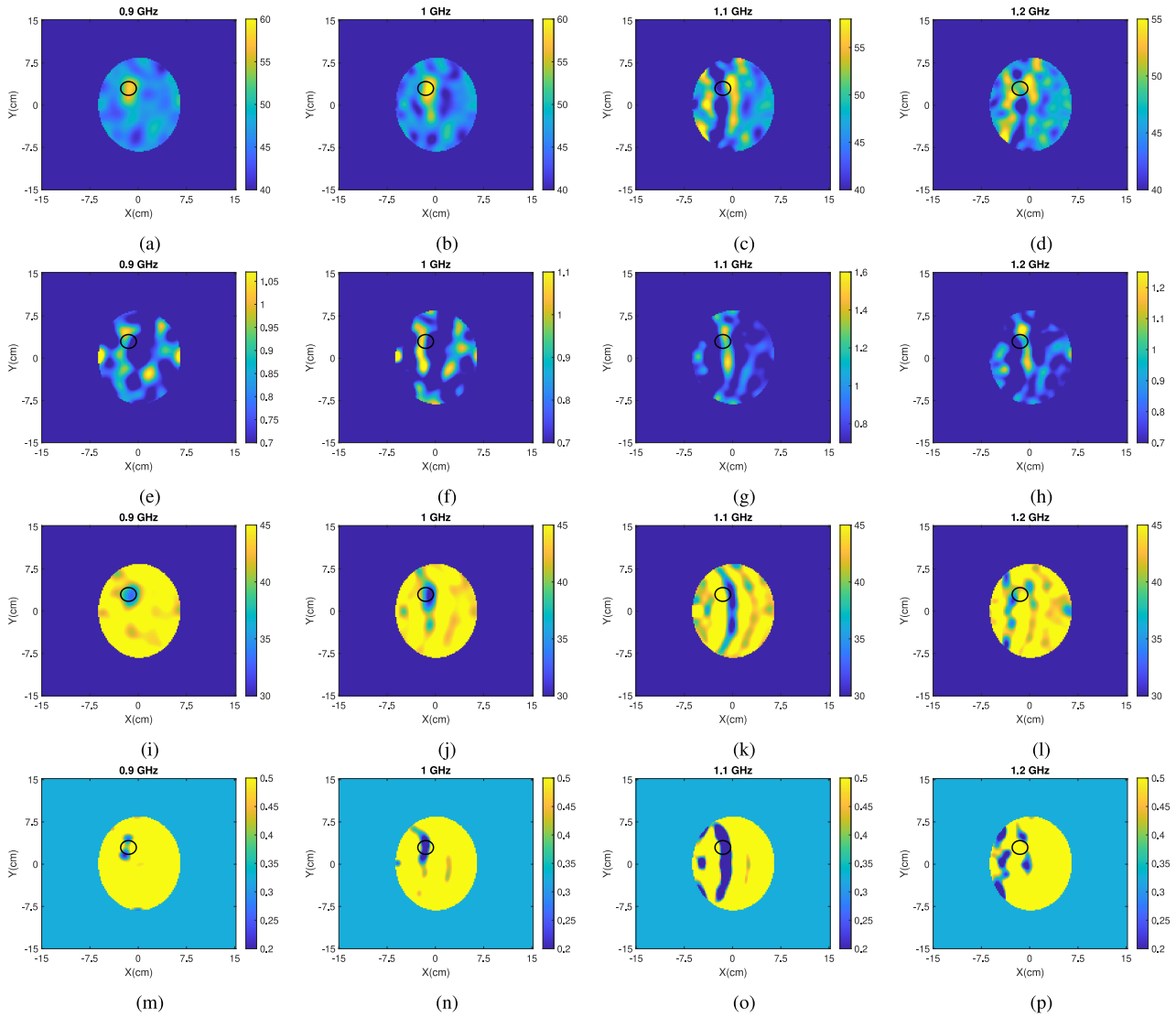

FIGURE 12. First row: CST reconstructed results of the permittivity for h-stroke using 3-D DBIM-TwIST; Second row: CST reconstructed results of the conductivity for h-stroke using 3-D DBIM-TwIST; Third row: CST reconstructed results of the permittivity for i-stroke using 3-D DBIM-TwIST; Fourth row: CST reconstructed results of the conductivity for i-stroke using 3-D DBIM-TwIST.

TABLE 4. Relative errors of the conductivity in the target area for the 2-D examined scenarios.

	0.9 GHz	1.0 GHz	1.1 GHz	1.2 GHz
CST h-stroke	0.4717	0.4586	0.4195	0.477
CST i-stroke	1.68	1.66	1.33	1.601
Exp h-stroke	0.4644	0.4687	0.4750	0.4595
Exp i-stroke	1.4939	1.4937	1.5228	1.624

TABLE 5. Relative errors of the permittivity in the target area for the 3-D examined scenarios.

	0.9 GHz	1.0 GHz	1.1 GHz	1.2 GHz
CST h-stroke	0.1236	0.1271	0.244	0.1906
CST i-stroke	0.9714	1.0099	1.3393	1.2201
Exp h-stroke	0.096	0.1081	0.1241	0.1277
Exp i-stroke	1.4114	1.3885	1.3826	1.29

TABLE 6. Relative errors of the conductivity in the target area for the 3-D examined scenarios.

	0.9 GHz	1.0 GHz	1.1 GHz	1.2 GHz
CST h-stroke	0.4524	0.438	0.373	0.4482
CST i-stroke	2.2492	1.7673	1.7737	3.09
Exp h-stroke	0.6892	0.6587	0.6166	0.4834
Exp i-stroke	2.7054	2.7975	3.1453	3.1617

V. CONCLUSION

We have examined the performance of a MWI setup for the problem of brain stroke detection and differentiation, using the 2-D and 3-D DBIM-TwIST algorithm and a novel, anatomically accurate, multi-layer head phantom. We called this a Zubal model, as it extends a slice from the Zubal numerical phantom to create 3-D moulds that can be combined to construct the final phantom. We note that the phantom is an extended 2-D cut of the head surrounded by a 2-D configuration of antennas, which was confined to a ring by our experimental setup. This phantom and antenna configuration allow a 2-D inversion to produce results of

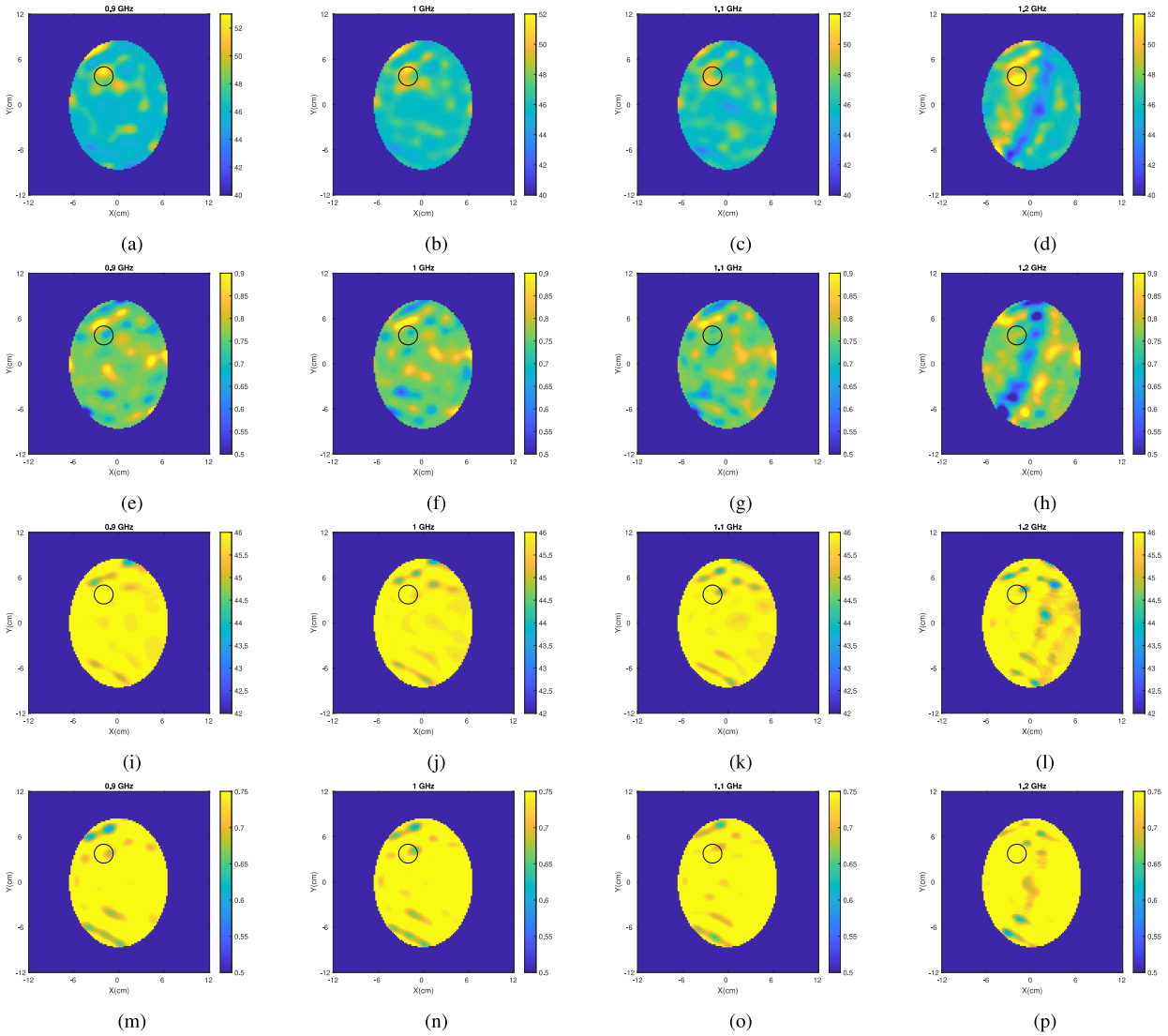

FIGURE 13. First row: Experimental reconstructed results of the permittivity for h-stroke using 2-D DBIM-TwIST; Second row: Experimental reconstructed results of the conductivity for h-stroke using 2-D DBIM-TwIST; Third row: Experimental reconstructed results of the permittivity for i-stroke using 2-D DBIM-TwIST; Fourth row: Experimental reconstructed results of the conductivity for i-stroke using 2-D DBIM-TwIST.

comparable accuracy. However, it is still critical to validate the 3-D algorithm for such scenarios by comparing with 2-D images, and this has been the main objective of this study. In our next experiments, we will extend the brain phantom to include a variation in the third dimension, and our antenna array will contain more than one ring. Preliminary simplified simulations of this scenario in Section III have shown the superior performance of the 3-D algorithm.

The phantom mimics the high dielectric difference in the brain tissues by comprising gelatine-based phantoms that mimic the dielectric permittivity of various head tissues. Importantly, we used a construction process that eliminates the presence of plastic in the phantom, which would distort the signals processed by our algorithm.

We placed the phantom in our experimental prototype as well as in a CST model that simulates the experiment. CST simulation results indicated that we are able to successfully localize and differentiate stroke targets by estimating their dielectric properties. Our measured data reconstructions confirmed that stroke detection and differentiation are more challenging with experimental data. Results for the hemorrhagic-like target were more accurate than for the ischemic-like target as the latter has a lower dielectric contrast with the surrounding brain matter. In accordance with previous work [18], we observed that permittivity estimation is more accurate than conductivity estimation. Importantly, we also observed that the differences in the dielectric estimation of i-stoke and h-stroke targets is higher if reconstructions are performed with the 3-D DBIM-TwIST algorithm.

We also note that our calibration method relies on the signal difference between the experimental and the simulated

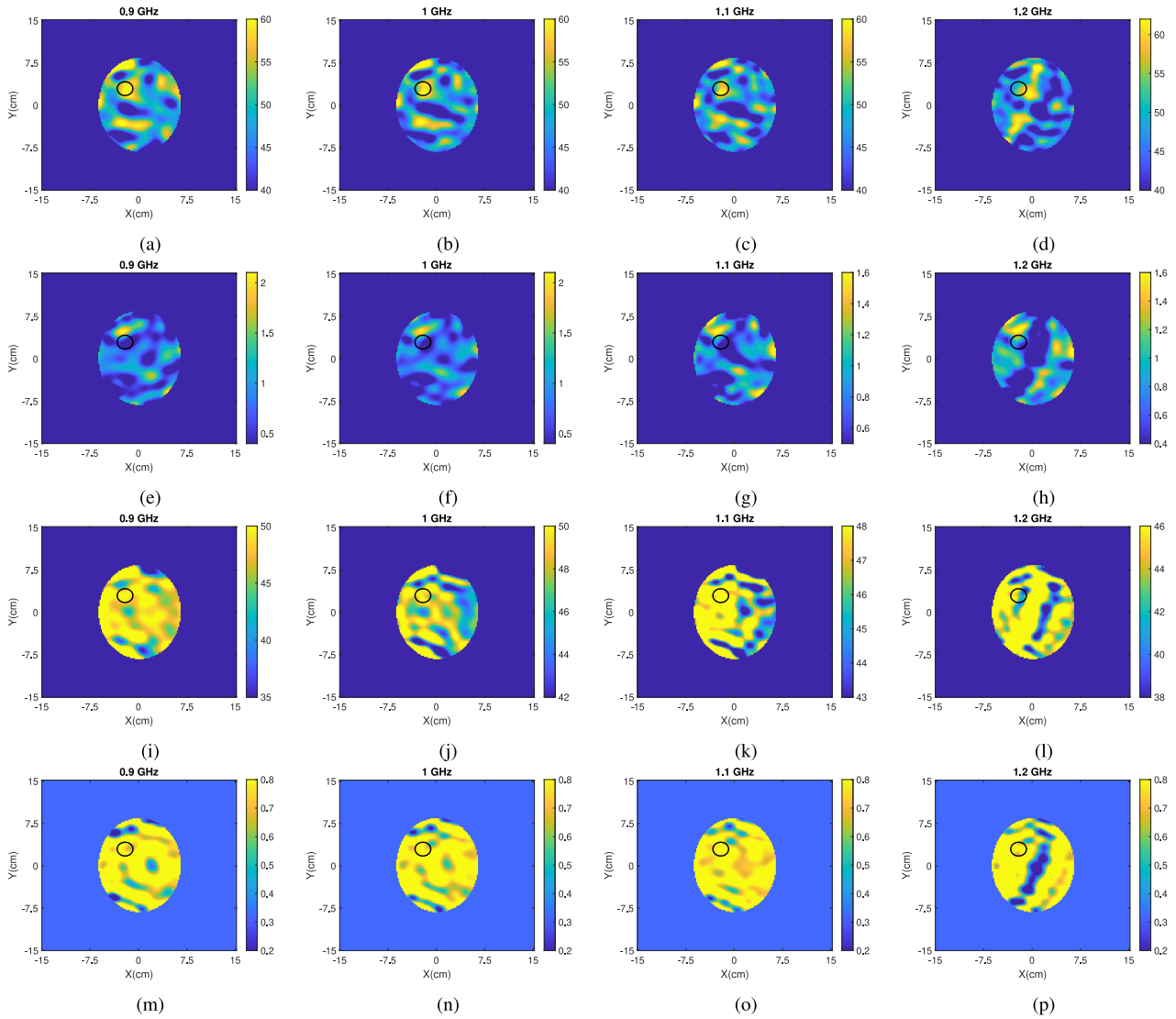

FIGURE 14. First row: Experimental reconstructed results of the permittivity for h-stroke using 3-D DBIM-TwIST; Second row: Experimental reconstructed results of the conductivity for h-stroke using 3-D DBIM-TwIST; Third row: Experimental reconstructed results of the permittivity for i-stroke using 3-D DBIM-TwIST; Fourth row: Experimental reconstructed results of the conductivity for i-stroke using 3-D DBIM-TwIST.

NT scenarios. As an exact NT model is not realistic for clinical scenarios, we aim to further examine if calibrating with an accurate approximate NT scenario compared to a full NT scenario is feasible. Our recent work at [54] has examined what prior knowledge is needed to successfully differentiate the two types of the stroke when using a complex model, and whether an improved forward model could produce better image quality. Our early results indicated that the addition of thin head layers in the forward model is not critical for the successful reconstruction of the target's dielectric properties.

The purpose of this study was to experimentally validate our 2-D and 3-D DBIM-TwIST algorithms for stroke detection and differentiation, but also to further assess experimentally the performance of the 3-D algorithm for the examined application. For some of the studied scenarios, the 2-D DBIM-TwIST can lead to more accurate reconstructions. This is because the 2-D inverse problem approximates well the 3-D problem in these cases, and it is less ill-posed than the 3-D inverse problem as it contains a much smaller number of unknowns. However, and as showed by our numerical results with 2 rings of antennas and a smaller target placed between the two rings, the 3-D inverse algorithm can provide more accurate results for problems with significant variation along all three dimensions, as can be the case of brain imaging.

Our future work will focus on improving the system's performance by using tools such as frequency hopping, optimization of the initial guess through a two-step reconstruction process. These tools have shown to be very effective in previous work in microwave breast imaging [43]. Pre-processing methods to discard data which

are associated with measurement errors can also improve performance [55], [56]. Furthermore, we aim to validate the DBIM-TwIST in more realistic scenarios using the Zubal model, where targets of different sizes are located in various positions and not aligned with the antenna height.

REFERENCES

[1] S. S. Virani *et al.*, "Heart disease and stroke statistics—2020 update: A report from the American heart association," *Circulation*, vol. 141, no. 9, pp. e139–e596, 2020.

[2] V. L. Feigin, "Stroke epidemiology in the developing world," *Lancet*, vol. 365, no. 9478, pp. 2160–2161, 2005.

[3] D. J. Mollura and M. P. Lungren, *Radiology in Global Health*. New York, NY, USA: Springer, 2014.

[4] K. B. Walsh, "Non-invasive sensor technology for prehospital stroke diagnosis: Current status and future directions," *Int. J. Stroke*, vol. 14, no. 6, pp. 592–602, 2019.

[5] L. Alon and S. Dehkharghani, "A stroke detection and discrimination framework using broadband microwave scattering on stochastic models with deep learning," 2021, *arXiv:2104.06543*.

[6] R. Chandra, H. Zhou, I. Balasingham, and R. M. Narayanan, "On the opportunities and challenges in microwave medical sensing and imaging," *IEEE Trans. Biomed. Eng.*, vol. 62, no. 7, pp. 1667–1682, Jul. 2015.

[7] S. Gabriel, R. Lau, and C. Gabriel, "The dielectric properties of biological tissues: II. Measurements in the frequency range 10 hz to 20 GHz," *Phys. Med. Biol.*, vol. 41, no. 11, p. 2251, 1996.

[8] S. Gabriel, R. W. Lau, and C. Gabriel, "The dielectric properties of biological tissues: III. Parametric models for the dielectric spectrum of tissues," *Phys. Med. Biol.*, vol. 41, no. 11, p. 2271, 1996.

[9] J. A. T. Vasquez *et al.*, "A prototype microwave system for 3D brain stroke imaging," *Sensors*, vol. 20, no. 9, p. 2607, 2020.

[10] J.-C. Bolomey, "Crossed viewpoints on microwave-based imaging for medical diagnosis: From genesis to earliest clinical outcomes," in *The World of Applied Electromagnetics*. Cham, Switzerland: Springer Int., 2018, pp. 369–414.

[11] M. Azghani, P. Kosmas, and F. Marvasti, "Microwave medical imaging based on sparsity and an iterative method with adaptive thresholding," *IEEE Trans. Med. Imag.*, vol. 34, no. 2, pp. 357–365, Feb. 2015.

[12] P. Kosmas and L. Crocco, "Introduction to special issue on 'electromagnetic technologies for medical diagnostics: Fundamental issues, clinical applications and perspectives"' *Diagnostics*, vol. 9, no. 1, p. 19, 2019.

[13] P. M. Meaney, M. W. Fanning, D. Li, S. P. Poplack, and K. D. Paulsen, "A clinical prototype for active microwave imaging of the breast," *IEEE Trans. Microw. Theory Techn.*, vol. 48, no. 11, pp. 1841–1853, Nov. 2000.

[14] S. Candefjord *et al.*, "Microwave technology for detecting traumatic intracranial bleedings: Tests on phantom of subdural hematoma and numerical simulations," *Med. Biol. Eng. Comput.*, vol. 55, no. 8, pp. 1177–1188, 2017.

[15] A. T. Mobashsher and A. M. Abbosh, "On-site rapid diagnosis of intracranial hematoma using portable multi-slice microwave imaging system," *Sci. Rep.*, vol. 6, no. 1, pp. 1–17, 2016.

[16] A. S. M. Alqadami, K. S. Bialkowski, A. T. Mobashsher, and A. M. Abbosh, "Wearable electromagnetic head imaging system using flexible wideband antenna array based on polymer technology for brain stroke diagnosis," *IEEE Trans. Biomed. Circuits Syst.*, vol. 13, no. 1, pp. 124–134, Feb. 2019.

[17] I. Merunka, A. Massa, D. Vrba, O. Fiser, M. Salucci, and J. Vrba, "Microwave tomography system for methodical testing of human brain stroke detection approaches," *Int. J. Antennas Propag.*, vol. 2019, Mar. 2019, Art. no. 4074862.

[18] O. Karadima *et al.*, "Experimental validation of microwave tomography with the DBIM-TwIST algorithm for brain stroke detection and classification," *Sensors*, vol. 20, no. 3, p. 840, 2020.

[19] S. Ahsan *et al.*, "Design and experimental validation of a multiple-frequency microwave tomography system employing the DBIM-TwIST algorithm," *Sensors*, vol. 18, no. 10, p. 3491, 2018.

[20] M. S. R. Bashri and T. Arslan, "Low-cost and compact RF switching system for wearable microwave head imaging with performance verification on artificial head phantom," *IET Microwav. Antennas Propag.*, vol. 12, no. 5, pp. 706–711, 2018.

[21] C. Yu *et al.*, "Active microwave imaging II: 3-D system prototype and image reconstruction from experimental data," *IEEE Trans. Microw. Theory Techn.*, vol. 56, no. 4, pp. 991–1000, Apr. 2008.

[22] M. Persson *et al.*, "Microwave-based stroke diagnosis making global prehospital thrombolytic treatment possible," *IEEE Trans. Biomed. Eng.*, vol. 61, no. 11, pp. 2806–2817, Nov. 2014.

[23] P. M. Meaney *et al.*, "Initial clinical experience with microwave breast imaging in women with normal mammography," *Acad. Radiol.*, vol. 14, no. 2, pp. 207–218, 2007.

[24] M. Hopfer, R. Planas, A. Hamidipour, T. Henriksson, and S. Semenov, "Electromagnetic tomography for detection, differentiation, and monitoring of brain stroke: A virtual data and human head phantom study," *IEEE Antennas Propag. Mag.*, vol. 59, no. 5, pp. 86–97, Oct. 2017.

[25] D. Cook *et al.*, "Case report: Preliminary images from an electromagnetic portable brain scanner for diagnosis and monitoring of acute stroke," *Front. Neurol.*, vol. 12, p. 2016, Oct. 2021.

[26] R. Scapaticci, L. Di Donato, I. Catapano, and L. Crocco, "A feasibility study on microwave imaging for brain stroke monitoring," *Progr. Electromagn. Res. B*, vol. 40, pp. 305–324, May 2012.

[27] R. Scapaticci, J. Tobon, G. Bellizzi, F. Vipiana, and L. Crocco, "Design and numerical characterization of a low-complexity microwave device for brain stroke monitoring," *IEEE Trans. Antennas Propag.*, vol. 66, no. 12, pp. 7328–7338, Dec. 2018.

[28] L. Crocco, I. Karanasiou, M. L. James, and R. C. Conceição, *Emerging Electromagnetic Technologies for Brain Diseases Diagnostics, Monitoring and Therapy*. Cham, Switzerland: Springer Int., 2018.

[29] O. Karadima, N. Ghavami, I. Sotiriou, and P. Kosmas, "Performance assessment of microwave tomography and radar imaging using an anthropomorphic brain phantom," in *Proc. 33rd Gen. Assembly Sci. Symp. Int. Union Radio Sci.*, Rome, Italy, 2020, pp. 1–4.

[30] N. Ghavami, G. Tiberi, D. J. Edwards, and A. Monorchio, "UWB microwave imaging of objects with canonical shape," *IEEE Trans. Antennas Propag.*, vol. 60, no. 1, pp. 231–239, Jan. 2012.

[31] J. D. Shea, P. Kosmas, S. C. Hagness, and B. D. Van Veen, "Three-dimensional microwave imaging of realistic numerical breast phantoms via a multiple-frequency inverse scattering technique," *Med. Phys.*, vol. 37, no. 8, pp. 4210–4226, 2010.

[32] A. Fedeli, C. Estatico, M. Pastorino, and A. Randazzo, "Microwave detection of brain injuries by means of a hybrid imaging method," *IEEE Open J. Antennas Propag.*, vol. 1, pp. 513–523, 2020.

[33] M. Salucci, A. Polo, and J. Vrba, "Multi-step learning-by-examples strategy for real-time brain stroke microwave scattering data inversion," *Electronics*, vol. 10, no. 1, p. 95, 2021.

[34] F. Wang *et al.*, "Experimental study on differential diagnosis of cerebral hemorrhagic and ischemic stroke based on microwave measurement," *Technol. Health Care*, vol. 28, no. S1, pp. 289–301, 2020.

[35] G. Zhu, A. Bialkowski, L. Guo, B. Mohammed, and A. Abbosh, "Stroke classification in simulated electromagnetic imaging using graph approaches," *IEEE J. Electromagn. RF Microwav. Med. Biol.*, vol. 5, no. 1, pp. 46–53, Mar. 2021.

[36] X. Chen, Z. Wei, M. Li, and P. Rocca, "A review of deep learning approaches for inverse scattering problems (invited review)," *Progr. Electromagn. Res.*, vol. 167, pp. 67–81, Jun. 2020.

[37] J. Xu *et al.*, "Noninvasive and portable stroke type discrimination and progress monitoring based on a multichannel microwave transmitting–receiving system," *Sci. Rep.*, vol. 10, no. 1, pp. 1–13, 2020.

[38] M. Bertero and P. Boccacci, *Introduction to Inverse Problems in Imaging*. Boca Raton, FL, USA: CRC Press, 2020.

[39] H. Iida *et al.*, "Three-dimensional brain phantom containing bone and grey matter structures with a realistic head contour," *Ann. Nucl. Med.*, vol. 27, no. 1, pp. 25–36, 2013.

[40] S. Semenov, T. Huynh, T. Williams, B. Nicholson, and A. Vasilenko, "Dielectric properties of brain tissue at 1 GHz in acute ischemic stroke: Experimental study on swine," *Bioelectromagnetics*, vol. 38, no. 2, pp. 158–163,2016.

[41] V. Mariano, J. A. T. Vasquez, R. Scapaticci, L. Crocco, P. Kosmas, and F. Vipiana, "Comparison of reconstruction algorithms for brain stroke microwave imaging," in *Proc. IEEE MTT-S Int. Microw. Biomed. Conf. (IMBioC)*, Toulouse, France, 2020, pp. 1–3.

[42] A. Fedeli, V. Schenone, A. Randazzo, M. Pastorino, T. Henriksson, and S. Semenov, "Nonlinear S-parameters inversion for stroke imaging," *IEEE Trans. Microw. Theory Techn.*, vol. 69, no. 3, pp. 1760–1771, Mar. 2021.

[43] Z. Miao and P. Kosmas, "Multiple-frequency DBIM-TwIST algorithm for microwave breast imaging," *IEEE Trans. Antennas Propag.*, vol. 65, no. 5, pp. 2507–2516, May 2017.

[44] P. Lu and P. Kosmas, "Three-dimensional microwave head imaging with GPU-based FDTD and the DBIM method," *IEEE Trans. Comput. Imag.*, submitted for publication.

[45] P. Lu, J. Córcoles, and P. Kosmas, "Enhanced FEM-based DBIM approach for two-dimensional microwave imaging," *IEEE Trans. Antennas Propag.*, vol. 69, pp. 5187–5192, Aug. 2021.

[46] T. M. Grzegorczyk, P. M. Meaney, P. A. Kaufman, R. M. di Florio-Alexander, and K. D. Paulsen, "Fast 3-D tomographic microwave imaging for breast cancer detection," *IEEE Trans. Med. Imag.*, vol. 31, no. 8, pp. 1584–1592, Aug. 2012.

[47] Q. Fang, P. M. Meaney, and K. D. Paulsen, "Viable three-dimensional medical microwave tomography: Theory and numerical experiments," *IEEE Trans. Antennas Propag.*, vol. 58, no. 2, pp. 449–458, Feb. 2010.

[48] T. J. Colgan, S. C. Hagness, and B. D. Van Veen, "A 3-D level set method for microwave breast imaging," *IEEE Trans. Biomed. Eng.*, vol. 62, no. 10, pp. 2526–2534, Oct. 2015.

[49] D. Ireland and A. Abbosh, "Modeling human head at microwave frequencies using optimized debye models and FDTD method," *IEEE Trans. Antennas Propag.*, vol. 61, no. 4, pp. 2352–2355, Apr. 2013.

[50] A. M. Qureshi, Z. Mustansar, and A. Maqsood, "Analysis of microwave scattering from a realistic human head model for brain stroke detection using electromagnetic impedance tomography," *Progr. Electromagn. Res. M*, vol. 52, pp. 45–56, 2016.

[51] I. G. Zubal, C. R. Harrell, E. O. Smith, Z. Rattner, G. Gindi, and P. B. Hoffer, "Computerized three-dimensional segmented human anatomy," *Med. Phys.*, vol. 21, no. 2, pp. 299–302, 1994.

[52] T. Rydholm, A. Fhager, M. Persson, S. D. Geimer, and P. M. Meaney, "Effects of the plastic of the realistic geePS-L2S-breast phantom," *Diagnostics*, vol. 8, no. 3, p. 61, 2018.

[53] O. Karadima, P. Lu, and P. Kosmas, "Comparison of 2-D and 3-D DBIM-TwIST for brain stroke detection and differentiation," in *Proc. 15th Eur. Conf. Antennas Propag. (EuCAP)*, Dusseldorf, Germany, 2021, pp. 1–4.

[54] O. Karadima, P. Lu, I. Sotiriou, and P. Kosmas, "Evaluation of the initial guess for brain stroke detection using microwave tomography," in *Proc. IEEE Int. Conf. Antenna Meas. Appl. (CAMA)*, 2021, pp. 1–5.

[55] Z. Miao, P. Kosmas, and S. Ahsan, "Impact of information loss on reconstruction quality in microwave tomography for medical imaging," *Diagnostics*, vol. 8, no. 3, p. 52, 2018.

[56] P. Lu, J. Córcoles, and P. Kosmas, "Tools for the efficient implementation of the DBIM algorithm in microwave imaging experiments," in *Proc. 14th Eur. Conf. Antennas Propag. (EuCAP)*, Copenhagen, Denmark, 2020, pp. 1–4.